LAWRENCE
LIVERMORE
NATIONAL
LABORATORY

LLNL-JRNL-599793

BOUT simulations of drift resistive ballooning L-mode turbulence in the edge of the DIII-D tokamak

B. I. Cohen, M. V. Umansky, W. M. Nevins, M. Makowski, J. Boedo, D. Rudakov, G. McKee, Z. Yan, R. Groebner

November 8, 2012

Physics of Plasmas

Disclaimer

This document was prepared as an account of work sponsored by an agency of the United States government. Neither the United States government nor Lawrence Livermore National Security, LLC, nor any of their employees makes any warranty, expressed or implied, or assumes any legal liability or responsibility for the accuracy, completeness, or usefulness of any information, apparatus, product, or process disclosed, or represents that its use would not infringe privately owned rights. Reference herein to any specific commercial product, process, or service by trade name, trademark, manufacturer, or otherwise does not necessarily constitute or imply its endorsement, recommendation, or favoring by the United States government or Lawrence Livermore National Security, LLC. The views and opinions of authors expressed herein do not necessarily state or reflect those of the United States government or Lawrence Livermore National Security, LLC, and shall not be used for advertising or product endorsement purposes.

LLNL-JRNL-599793

Simulations of drift resistive ballooning L-mode turbulence in the edge plasma of the DIII-D tokamak

Bruce I. Cohen, Maxim V. Umansky, William M. Nevins, and M. A. Makowski

Lawrence Livermore National Laboratory

Livermore, CA 94551

Jose A. Boedo and Dmitry Rudakov

UC San Diego, San Diego, CA 92093

George R. McKee and Zheng Yan

University of Wisconsin-Madison, Madison, Wisconsin 53706

Richard J. Groebner and the DIII-D Collaboration

General Atomics, P.O. Box 85608 San Diego, CA 92186-5608

Results from simulations of electromagnetic drift-resistive ballooning turbulence for tokamak edge turbulence in realistic single-null geometry are reported. The calculations are undertaken with the BOUT three-dimensional fluid code that solves Braginskii-based fluid equations [X. Q. Xu, and R. H. Cohen, Contrib. Plasma Phys. 36 (1998) 158]. The simulation domain models the actual magnetic geometry of the DIII-D tokamak [J. L. Luxon *et al.*, Fusion Sci. Technol. **48**, 807 (2002)]. The computations track the development of drift-resistive ballooning turbulence in the edge region to saturation.

Fluctuation amplitudes, fluctuation spectra, and particle and thermal fluxes are compared to experimental probe and beam-emission-spectroscopy data for a few well-characterized L-mode discharges in DIII-D. Post-processing of the simulation data using synthetic diagnostics facilitates the comparisons. The simulations are comprised of a suite of runs in which the physics model is extended to include more fluid fields and physics terms. The simulations yield results for fluctuation amplitudes, correlation lengths, particle and energy fluxes and diffusivities in reasonable agreement with measurements near the outer midplane of the discharge, and the agreement improves as more physics is included in the model. Data from experiment and simulations show the stabilizing effects of sheared ExB poloidal rotation and of lower electron temperature and density.

I. INTRODUCTION

The edge region of tokamak plasmas continues to be an active research area because of its importance in influencing particle and energy confinement in the plasma as a whole,[1] the importance of the plasma interaction with the divertor plates and the wall of the vacuum vessel,[2] and the richness of the collective phenomena in the edge. The edge plasma is subject to plasma turbulence that degrades energy and particle confinement and can include transient events as in the Edge Localized Mode (ELM) as well as the formation of filamentary structures. Understanding steady-state, saturated turbulence in the tokamak edge plasma is challenging to theory and modeling. Direct numerical simulation has become a useful tool for exploring the physics of the turbulence observed in the tokamak edge because the physics and tokamak geometry are too complex for analytical theory. The direct simulation in realistic geometry of turbulence in L-mode discharges in the DIII-D tokamak[3] edge plasma is taken as a simple starting point toward understanding turbulence in tokamak edge plasmas. These L-mode discharges exhibit stationary steady-states and are less complex than H-mode discharges with ELM activity. In this work comparisons of the simulation results to DIII-D L-mode data from experimental diagnostics are reported.

Experimental observations and transport analysis have established that the edge region of L-mode tokamak plasmas exhibits anomalous transport of particles and energy.[4] There are strong gradients in the edge region that provide drive mechanisms for collective modes of instability that can lead to the observed anomalous transport. Antecedents for the work presented here are the earlier studies by Carreras and co-workers,[5,6] and by Guzdar, Drake and co-workers,[7,8,9,10,11] wherein resistive interchange,

resistive ballooning, and drift-resistive ballooning modes were considered. The theory of resistive interchange modes traces back to the earlier classic papers of Furth, et al.[12] and Coppi.[13] The references cited here are intended as representative examples of a larger body of work. The simulation results and focused comparison to L-mode discharge data from DIII-D reported here are based on the drift-resistive ballooning physics model evolved from the earlier work of Carreras, et al., and Guzdar, et al., using fluid equations solved numerically[14,15,16] in a realistic, single-null geometry for DIII-D for conditions specific to a series of well-characterized L-mode discharges. We make detailed comparisons of the simulation results to data provided by a scanning Langmuir probe[17] and by beam-emission spectroscopy (BES)[18] where available for DIII-D L-mode shots #119919, 119921, 119930, and 119934. Shots 119930 and 119934 have lower edge plasma density and electron temperature than in 119919/119921.

The principal results here are that simulations of the drift-resistive ballooning model yield fluctuation amplitudes, particle and heat fluxes, inferred transport coefficients, correlation lengths, and spectra that are in reasonable agreement with the experimental data. Moreover, the agreement tends to improve as the equation set in the simulation is made more complete.

The paper is organized as follows. The Introduction is followed in Sec. II by a description of the model equations and the simulation methodology. Section III presents a discussion of the simulation results and the diagnostics in the simulations, and comparison to the experimental data. The paper concludes in Sec. IV with a summary discussion.

II. MODEL EQUATIONS FOR EDGE TURBULENCE

The model equations for fluid turbulence in tokamak edge region are predicated on the validity of the assumption that the edge plasma is sufficiently collisional. The Braginskii[19] two-fluid equations for a strongly magnetized, collisional plasma provide the basis of the equation set in the simulations. They are expressed here in drift ordering:[20,21,22]

$$\frac{d\tilde{N}_i}{dt} + \nabla N_i \tilde{V}_{\|} = \left(\frac{2c}{eB}\right) b_0 \times \kappa \bullet (\nabla \tilde{P}_e - N_i e \nabla \varphi) + \nabla_{\|}(\tilde{j}_{\|}/e) \quad (1a)$$

$$\frac{d\varpi}{dt} = 2\omega_{ci} b_0 \times \kappa \bullet \nabla \tilde{P} \quad + \quad N_{i0} Z_i e \frac{4\pi V_A^2}{c^2} \nabla_{\|} \tilde{j}_{\|} \quad (1b)$$

$$\frac{d\tilde{V}_{\|e}}{\partial t} = -\frac{e}{m_e} E_{\|} - \frac{1}{N_{i0} m_e} (T_{e0} \nabla_{\|} \tilde{N}_i) + 0.51 \nu_{ei} \tilde{j}_{\|} \quad (1c)$$

$$\frac{d\tilde{V}_{\|i}}{dt} = -\frac{1}{N_{i0} M_i} \nabla_{\|} \tilde{P}, \quad (1d)$$

$$\frac{d\tilde{T}_e}{dt} = \frac{2}{3N_{i0}} \nabla \bullet \left(\kappa_{\|}^e \nabla_{\|} \tilde{T}_e\right), \quad \kappa_{\|}^e = 3.2 \frac{N_{i0} T_{e0} \tau_{e0}}{m_e} \quad (1e)$$

$$\mathbf{E} = -\tfrac{1}{c}\tfrac{\partial}{\partial t}\mathbf{A}_{\|} - \nabla\varphi, \quad -\nabla_{\perp}^2 \mathbf{A}_{\|} = \tfrac{4\pi}{c}\mathbf{j}_{\|}, \quad \mathbf{B} = \nabla \times \mathbf{A}_{\|} + \mathbf{B}_0 \quad (1f)$$

where

$$\varpi = \nabla \cdot \left[e Z_i N_i \nabla \varphi\right] \approx e Z_i N_{i0} \nabla^2 \varphi \quad (2a)$$

$$\nabla_{\|} = \mathbf{b}_0 \cdot \nabla + \tilde{\mathbf{b}} \cdot \nabla \quad (2b)$$

$$\frac{d}{dt} = \frac{\partial}{\partial t} + \mathbf{V}_E \bullet \nabla \quad (2c)$$

$$Z_i = 1, \quad N_i = N_{i0} + \tilde{N}_i, \quad T_s = T_{s0} + \tilde{T}_s, \ldots \quad (2d)$$

$$\tilde{P} = N_{i0}(\tilde{T}_e + \tilde{T}_i) + \tilde{N}_i (T_{e0} + T_{i0}), \quad (2e)$$

$$T_{i0} = T_{e0}, \ \tilde{T}_i = 0, \quad V_{\|s0} = 0 \quad (2f)$$

and $\tilde{N}_i$ is the ion fluctuation density, $N_i = N_{i0} + \tilde{N}_i$ is the total ion density, ϖ is the vorticity, $\tilde{V}_{\|s}$ is the species *s* fluid velocity parallel to the unperturbed magnetic field, $T_s = T_{s0} + \tilde{T}_s$ relates the total species temperature to the unperturbed and fluctuating temperature components, **E** is the total electric field, $\mathbf{A}_{\|}$ is the fluctuating vector potential oriented parallel to the unperturbed magnetic field, **B** is the total magnetic field, $\mathbf{B}_0$ is the

unperturbed magnetic field, $\tilde{P}$ is the total pressure fluctuation, $\mathbf{V}_E$ is the $\mathbf{E}\times\mathbf{B}$ velocity in the total fields including fluctuations, e is the electron charge, Z_i is the effective ion charge taken to be unity throughout this study, $\kappa^{e,i}_{||}$ is the electron/ion parallel thermal conduction, and $\tilde{j}_{||} = \sum_s q_s N_s \tilde{v}_{||s}$ is the fluctuating parallel current. If ion temperature fluctuations are included, then there is an additional equation that mimics Eq.(1e), but written for the ions and which uses the Braginskii parallel thermal conduction for the ions[19] and replaces Eq.(2f) for the ion temperature fluctuations.

A suite of equation sets with increasing complexity based on Eqs.(1) and (2) is employed in the simulations reported here. In Case 1 the electron and ion temperature fluctuations are suppressed, and $\tilde{\mathbf{b}}\cdot\nabla$ is dropped in Eq.(2b). This is the simplest model in the suite that supports the resistive drift ballooning mode. In Case 2 the electron temperature fluctuation is included, but with $\kappa^{e}_{||}$=0, and $\tilde{\mathbf{b}}\cdot\nabla$ is dropped in Eq.(2b). Case 3 adds finite $\kappa^{e}_{||}$ to Case 2. Case 4 includes $\tilde{\mathbf{b}}\cdot\nabla$ in Eq.(2b) and is otherwise the same as Case 3. Case 5 adds ion temperature fluctuations to Case 4. Case 6 adds an imposed radial electric field fitted to experimental data to the background fields in Case 5. Simulations with an imposed radial electric field included in Case 1 were also conducted.

The numerical solution of Eqs.(1) and (2) in BOUT or BOUT++ (BOUT++ is the C++ language extended version of BOUT) is described in the published literature, Refs. (14-16), (22), and in literature accessible on the BOUT website (bout.llnl.gov). The present study uses BOUT, but the same equation set will be implemented in the more modern BOUT++ framework in future work. The equations are solved as an initial-value problem on a three-dimensional mesh. For tokamak simulations, quasi-ballooning coordinates are used with twist-shift periodic boundary conditions wrapping around the

torus toroidally and poloidally, and with Neumann (zero gradient) or Dirichlet (zero value) radial boundary conditions. A periodic toroidal wedge is simulated, typically 1/16 or 1/25 of the torus in the simulations. The grid dimensions are 64 toroidal cells in the wedge, 40 radial cells, and 64 poloidal cells. The radial domain size in the midplane is approximately $0.98 \leq R/R_{sep} \leq 1.03$, where R_{sep} is the major radius at the location of the magnetic separatrix (or in terms of the magnetic flux $0.9\psi_{norm}$ to $1.15\psi_{norm}$). When the size of the toroidal wedge is increased by 2x and the number of toroidal cells is increased by 2x to maintain the same toroidal resolution, there is no substantial change in the simulation results; detailed grid convergence studies are deferred to future work. The unperturbed profiles for the field quantities are input into the simulation using reconstructions based on experimental data, and the spatial mesh is defined with the use of the UEDGE code.[23] In the simulations fixed unperturbed axisymmetric (no toroidal variation) profiles are imposed for the density, temperatures, and, in some simulations, the electric potential. Nonlinear coupling back to the axisymmetric modes is dropped. In the future this assumption will be relaxed to study the effects of self-consistent zonal flows. Various benchmarks to verify the BOUT code are documented in published literature or on the BOUT website. We repeated a benchmark study with BOUT simulating the resistive ballooning mode instability and verified the results by comparing to the 2DX eigenvalue code results.[24]

In using the BOUT or BOUT++ frameworks for sets of fluid equations solved with finite-difference methods, occasionally a finite-amplitude spatial oscillation in the fluctuating fields is observed at the shortest spatial wavelength along the field line, an "odd-even" mode. The odd-even numerical mode is controlled in the simulations reported

here by inclusion of a fourth-order numerical viscosity term $-\alpha\nabla_{\|}^{4}$ (or higher even derivative) on the right sides of Eqs.(1a)-(1e) with α chosen so that the Nyquist mode has amplification factor less than unity while the physical modes of interest at longer parallel wavelength are negligibly influenced by the numerical viscosity. The origin of the odd-even mode may be associated with computing quadratic products of $\nabla_{\|}$ operators that are represented by centered three-point stencils in one dimension $\nabla f \approx \left(f_{j+1} - f_{j-1}\right)/\left(2\Delta x\right)$, because this representation leads to a centered five-point stencil for $\nabla^2 \approx \left(\left(f_{j+2} - f_j\right) - \left(f_j - f_{j-2}\right)\right)/\left(2\Delta x\right)^2 = \left(f_{j+2} - 2f_j + f_{j-2}\right)/\left(2\Delta x\right)^2$ with $f_{j\pm1}$ absent from the stencil. This finite-difference representation of the Laplacian has a finite null-space. The finite null-space can give rise to a numerical contamination, i.e., the odd-even mode. Other possible remedies for the odd-even contamination are staggering the mesh or using products of one-sided difference operators to alter the stencil of the second derivative.

III. SIMULATIONS OF EDGE PLASMA TURBULENCE IN L-MODE DISCHARGES AND COMPARISON TO EXPERIMENTAL DATA

A. Simulations of resistive drift ballooning in DIII-D shot #119919

We used the plasma profiles from the DIII-D database for the L-mode discharge #119919, constructed the BOUT mesh using UEDGE, and conducted a suite of simulations for the cases defined in Sec. II. Figures 1-5 show results comparing Cases 4 (includes T_e fluctuations but not T_i fluctuations) and 5 (includes both T_e and T_i fluctuations). Case 5 exhibits a faster linear growth rate (Fig. 1) and saturates at modestly higher amplitudes than does Case 4 without T_i fluctuations. With the unperturbed equilibrium gradients fixed and zonal flow generation precluded, the

saturated steady states observed may result from the nonlinear terms in Eqs.(1) mediating a balance between the linearly unstable modes and the damped modes with finite toroidal mode numbers. Such a mechanism for saturation of fluid turbulence is well established in the fluid dynamics and plasma physics literature.[25]

At saturation (Figs. 2-5) the turbulence is dominant on the outboard side of the tokamak, peaks near the outer midplane and near the separatrix, and extends a few centimeters on either side of the separatrix. The relative electron density fluctuations reach 20-30% (Fig. 2), and the electron temperature fluctuations are of order 50% (Fig. 3). The electron turbulent particle and thermal fluxes are likewise localized (Figs. 4 and 5) and are dominant on the outboard side and very small on the inboard side. There is a poloidal asymmetry in the fluctuations, which is apparently caused by the curvature drive on the outer side of the plasma and is consistent with experimental observations on the Alcator C-Mod tokamak.[26] In addition, there is an apparent up-down asymmetry, which is associated with the presence of the single X point in the plasma at the bottom of the cross section and the influence of the X point on the magnetic shear.

Tables I and II summarize the key observables at saturation in the simulations corresponding to the various cases defined in Sec. II. The conductive heat flux in Table I is defined as $\frac{3}{2}N_0 < \hat{v}_r \tilde{T}_e >_{tor,t}$, and the corresponding thermal diffusivity for just the conductive component of the heat flux is $\chi_e = -\frac{3}{2}N_0 < \tilde{v}_r \tilde{T}_e >_{tor,t} / N_0 \nabla T_{e0}$. The convective electron heat flux $\frac{3}{2}T_e < \tilde{N}_e \tilde{v}_r >_{tor,t}$, where $\tilde{N}_e \approx Z_i \tilde{N}_i$, is additive to the conductive component to compute the total heat flux. The effective electron density diffusivities, $D_r \equiv -\langle N_i V_r \rangle / \nabla_r N_{i0}$, reach 1-2 m^2/s; and the effective electron conductive thermal diffusivities are 2-6 m^2/s in these simulations (1-2 m^2/s near the separatrix).

The simulation results shown throughout corresponding to snapshots of fluctuations as functions of radius at saturation or the end of the simulation have been averaged in the z coordinate in BOUT, but still have a temporal variability of ±20-50%, which should be kept in mind when comparing the simulation data to experiment. The experimental data for the probe has error bars of a few percent.

B. Comparison of simulation results to experimental data for shot #119919

Shot #119919 in DIII-D is a well-characterized L-mode shot that exhibited steady-state turbulence. Simulation results are compared to data from a scanning Langmuir probe[17] and from beam emission spectroscopy (BES)[18] in Tables I and II respectively, and in Figs. 6 and 7, respectively. There is no BES data for #119919, and the BES data is for shot #119921, which has the same general plasma conditions as for #119919. The relative agreement of the simulations for Cases 4, 5 and 6 with respect to the experiment is fairly good in many respects. In comparing the simulations to the BES data, it is important to take into account the restrictions on spatial resolution set by the BES imaging grid, which has 1 cm separation radially and toroidally in its 4×4 approximately square grid. This restriction on spatial resolution necessitates processing the simulation data through a low-pass filter that mimics the 1 cm limit in resolution. This is accomplished by making use of the GKV software.[27] Spatial filtering (1D or 2D) is required in the simulation diagnostics to model the Δx=1 cm limit on spatial resolution in the BES. Filtering is applied to both the radial and binormal coordinates through the convolution of the data with a window function:

$$f_{smooth}(x) = \int dx' w(x-x') f(x'), \text{ where } w(x) = \begin{cases} \frac{1}{2\Delta x}\left[1+\cos\left(\frac{\pi x}{\Delta x}\right)\right] & \left|\frac{x}{\Delta x}\right| < 1 \\ 0 & \left|\frac{x}{\Delta x}\right| > 1 \end{cases} \quad (3)$$

Correlation functions are defined by normalized integrals:

$$C(f;x,t) = \frac{\iint dx'\,dt'\,f(x',t')\,f(x'-x,t'-t)}{\iint dx'\,dt'\,f(x',t')\,f(x',t')} \tag{4}$$

Simulation results for Case 5 with T_e and T_i fluctuations agree with the probe data for the peak values and relative localization of the density and electron temperature fluctuations and the radial particle flux for 2.23m ≤ R ≤ 2.29m in Fig. 6 to better than factors of 2, while the peak value of the electron conductive heat flux in the simulation is significantly larger than the probe data. However, the convective component of the electron heat flux measured by the probe ~2.4×10^4 J m^{-2} s^{-1} is in good agreement with the simulation and is much larger than the conductive heat flux, so that the agreement between the simulation and the probe on the total electron heat flux is better than a factor of 2. The particle and energy diffusivities in the simulations for Case 5 are in reasonable agreement with the diffusivities used in two-dimensional UEDGE simulations[28] to match experimental data for profiles (Table I).

The agreement of the filtered simulation data with BES data shown in Fig. 7 is better than a factor of 2 for the relative density fluctuation amplitude and localization, and for the peak of the density fluctuation power spectrum and its width. The radial half-width of the filtered density correlation function in the simulation is O(1/3) of that measured by BES. The overall comparison of the simulation results with the probe and BES data in Tables I and II shows that the agreement generally improves as more physics is added in the progression from Case 1 to 5.

Next, the influence of an imposed radial electric field E_r on the edge turbulence is investigated. The model of E_r used here is based on fitting an axisymmetric scalar electric potential to charge-exchange re-emission (CER)[29] and edge Langmuir probe data.

Because the domain extends to smaller radii than is accessible to the probe, extrapolation of the structure of the E_r inferred from the probe to smaller radii in such a way as to fit the CER data is challenging. The CER data has temporal scatter and lower spatial resolution than does the Langmuir probe. The model for E_r retains terms in a polynomial expansion of the electric potential through the second radial derivative determined from a smooth fit to the probe data and extrapolates smoothly to smaller radii (Fig. 8). The detailed E_r structure from the probe data near the separatrix in the model is not retained in this fit. The CER data neither confirms nor refutes the structure seen in the probe data near the separatrix. The shearing rate determined by dV_E/dr in the model is shown in Fig. 8c. Note that the maximum shearing rate in the model is ~2.4×10^4 s^{-1}, which is significantly smaller (by a factor of 4) than the observed linear growth rates in the BOUT simulations which are $O(1)\times10^5$ s^{-1}. The temporal evolution of the root-mean-square electron density fluctuation and electric potential amplitudes for Case 1 (no temperature fluctuations) is shown in Fig. 9a with and without the imposed E_r. Similar plots are shown in Fig. 9b with the inclusion of the T_e fluctuation amplitude for Cases 4, 5, and 6. With E_r imposed, the linear growth rates are weaker; and saturation is delayed. Figure 9a shows that the fluctuation amplitudes are still drifting to higher values when the simulation with finite E_r was terminated. The simulations in Figure 9b show modest reductions in saturated amplitudes for finite E_r and substantial reductions for $5\times E_r$ for the durations of these simulations. The comparison of Case 6 with E_r to probe and BES data is not quite as good as for Case 5 (E_r =0) in Tables I and II. With $5\times E_r$ the maximum shearing rate now exceeds the observed growth rate in the absence of the sheared V_E; and the stabilizing

effect of the flow shear is profound (Fig. 9a and 9b), which is in keeping with the established paradigm.[30]

In Figure 10 a different visualization of the simulation results for Cases 5 and 6 for #119919 is provided. (Note: Figure 10 represents the probe and simulation data with respect to the BOUT radial position in the midplane of the BOUT simulation geometry as in Figs. 2-5, 8 and 14, which is offset by +1.5 cm from the probe radial position located a few cm below the midplane in Figs. 6, 12, and 15.) The vertical error bars on the simulation data in Fig. 10 represent the temporal variability of the fluctuation-related quantities in the saturated state. Other simulations have been undertaken with a different model E_r that show complete recovery of the saturation amplitudes obtained with E_r=0 when the simulation is run long enough. The long-time effects of an imposed E_r for this and other models of E_r merit further study in the future. Moreover, the contributions from self-consistent generation of zonal flows will be included in future work.

C. Comparison of simulation results to experimental data for shot #119934

Simulation results and data from DIII-D L-mode discharges #119930 and #119934 with different plasma conditions in the same series are also compared. Plots of the radial ion density and electron temperature profiles for #119919, 119930 and 119934 are exhibited in Fig. 11. The profiles for #119930 and 119934 are similar to one another and are colder, lower-density discharges than in #119919. Discharge #119934 is more collisional than #119919 because of the stronger dependence of the collision frequency on the temperature. The growth rate for resistive ballooning from Eq.(31) of Ref. 6 scales as $\eta^{1/3}\beta^{2/3}/n^{1/3} \propto T^{1/6}n^{1/3}$, where η is the classical electrical resistivity, β is the ratio of kinetic energy density to magnetic energy density, T is the temperature (assume $T_e \approx T_i$)

and n is the plasma density. Hence, for ~50% reduced temperature and plasma density, the resistive ballooning growth rate is expected to decrease by $1/\sqrt{2}$; and this is consistent with the simulation results here. In Fig. 12 are plotted the experimental electron density and electron temperature fluctuation amplitudes, the radial electron particle flux, and the total electron thermal flux as functions of major radius from the probe data near the midplane. In Fig. 12 the fluctuation amplitudes and fluxes are similar in shots #119930 and 119934, and smaller than in shot #119919 consistent with expectation based on consideration of the resistive ballooning growth rate. This is reinforced by the results of the simulations of Case 5 with T_e and T_i fluctuations for shots #119919 and #119934 whose temporal evolution (Fig. 13) shows modestly reduced growth rates (reductions of ~20%) and somewhat lower RMS fluctuation amplitudes in the midplane for shot #119934. In comparing Figs. 6 and 14, it can be seen that the turbulent fluctuations extend to larger radii in the colder, more collisional #119934 plasma. Radial plots of the fluctuation amplitudes and fluxes in the BOUT midplane at saturation from the Case 5 simulation with T_e and T_i fluctuations are also compared to probe data from #119934 in Fig. 14.

In Fig. 15 are plotted the turbulent particle flux and the conductive and convective components of the energy fluxes as functions of the probe radial position for the Case 5 simulations (with $T_{e,i}$ fluctuations and E_r=0) of discharges #119919 and #119934. The fluxes are lower in the lower-temperature, lower-density #119934 plasma; and both simulations agree reasonably well with the probe data. The simulation and the probe data generally agree within a factor of 2 for the density and temperature fluctuations, the radial particle flux, and the electron total heat flux. Because the total particle flux in the

simulation agrees fairly well with the probe data, so does the convective heat flux; and the agreement of the total heat flux summed over the convective and conductive components between experiment and simulation is significantly better than for the conductive heat flux alone. The turbulence in the midplane peaks just inside the separatrix, apparently driven by the high gradients there.

In Fig. 16 is shown a simple fit of the radial electric field E_r to the probe and CER data for shot #119934. As with the fit of E_r to the data for shot #119919, the sharp structure seen in E_r in the probe data inside the separatrix is again omitted; and a smooth second radial derivative of the electric potential to smaller radii is extrapolated so that there is a good fit to the CER data at radii inside the separatrix. Deferred to future work is the incorporation into the model of the detailed structure of E_r near the separatrix seen by the probe. Comparisons of the results of BOUT simulation Case 6 with the inclusion of E_r to the results of Case 5 for shot #119934 are shown in the time history of the RMS fluctuation amplitudes in Fig. 17. The linear growth rate is reduced with the inclusion of E_r in the simulation, but the turbulence eventually recovers fluctuation amplitudes that are comparable to Case 5 with E_r=0 (Fig. 17). The density and electron temperature fluctuation amplitudes are modestly higher in the probe data than in the simulations, and the influence of finite E_r is weak (Fig. 14). The electron particle and total thermal fluxes based on the probe data cut through the simulation data (Fig. 15), and these fluxes at the end of the simulation shown in Fig. 17 are lower compared to the case with E_r=0 by factors of 2-4 in the case with finite E_r. Overall the agreement of the simulations with finite E_r and E_r=0, with the probe data is reasonably good for shot #119934.

An additional simulation of Case 6 (with electron and ion temperature fluctuations and E_r) for #119934 conditions was undertaken with a modification of the model equations, Eqs.(1) and (2), in which $A_{||}$=0, i.e., a purely electrostatic model for resistive drift ballooning. Given that the edge plasma is low beta (β<10^{-4} for T_e~50eV, n~10^{13}cm^{-3}, and B~2T where β is the ratio of thermal energy density to magnetic energy density) such that $\beta m_i/m_e$<<1, it is expected that the electromagnetic modifications should be weak. Indeed, the purely electrostatic simulation yields results for the turbulent fluctuations that differ less than 10-20% from the results from the electromagnetic model Case 6 results shown in in Figures 13 and 14, which is well within the temporal variability of the observables at saturation.

IV. CONCLUSIONS

In this work simulation results and focused comparison to L-mode discharge data from DIII-D in the edge region straddling the last closed flux surface are reported. This work can be viewed as a step toward validating the turbulence simulation using Braginskii-based plasma-fluid equations applied to the study of the edge turbulence in DIII-D L-mode discharges. These model equations are based on the drift-resistive ballooning physics model evolved from the earlier work of Carreras, et al., and Guzdar, et al., and implemented within the BOUT framework in a realistic, single-null geometry for DIII-D with conditions specific to a series of well-characterized L-mode discharges. We presented detailed comparisons of the simulation results to data provided by a scanning Langmuir probe[17] and by beam-emission spectroscopy (BES)[18] where available for DIII-D L-mode shots #119919, 119921, 119930, and 119934. Shots #119930 and #119934

have lower edge plasma density and electron temperature than in #119919/119921, and are found to be less unstable and less turbulent in both the experiment and the simulations. The simulations of shot #119934 yield growth rates ~20% less than those observed for the conditions of #119919, generally consistent with the 30% reduction in the resistive ballooning growth rate because of the lower temperature and density in discharge #119934. There are also results from a simulation of #119934 with an imposed E_r in which the physics model is purely electrostatic, and these results are substantially the same as those in the corresponding electromagnetic simulation. These results suggest that electromagnetic effects are generally unimportant for the low-β L-mode plasma conditions simulated.

The principal findings here are that simulations of the drift-resistive ballooning model yield results for fluctuation amplitudes, particle and heat fluxes, inferred radial diffusivities, correlation lengths, and spectra that are in reasonable agreement with the DIII-D L-mode experimental data. Moreover, the agreement tends to improve as the equation set in the simulation is made more complete in the progression from Case 1 to 5 (Tables I and II). Imposing a radial electric field in the simulations, based on a simple model fit to the probe and BES data from DIII-D, adds a sheared ExB flow that reduces the linear growth rates observed in the simulations. In the simulations of #119919 the saturated turbulence with finite E_r is at moderately smaller amplitudes, while in the simulations of #119934 with E_r the turbulence recovers and saturates at amplitudes very close to those observed with E_r=0. That the stabilizing effects of E_r on the turbulence and the saturation amplitudes are either modest or very weak is in keeping with the fact that the shearing rates due to E_r are much smaller than the linear growth rates. Remarkably,

for the imposed electric field E_r scaled up by a factor of 5 there is a drastic (several orders of magnitude) reduction in the saturated turbulence levels. This value of E_r corresponds to a shearing rate that is comparable to the linear growth rates and the turbulence characteristic frequencies, and this is where one would indeed expect the E_r shearing to have a strong effect. It is not yet understood why the turbulence fully recovers in the simulation of #119934 with E_r and not in the simulation of #119919 with E_r over the length of time simulated. One can speculate that the turbulence saturation mechanisms here are different from the linear growth reduction mechanisms. The E_r model used in the present simulation is not self-consistent, and this should be considered only as a first step. It is not clear if inclusion of self-consistent zonal flows will further reduce the turbulence amplitudes at saturation. Saturation effected by nonlinear coupling between linearly unstable and linearly damped modes may be sufficiently robust for the conditions considered here that inclusion of self-generated zonal flows will have little effect. To investigate this, future work will include modeling of self-consistent zonal flow effects with an appropriate algorithm to maintain the background gradients at long wavelengths.[31]

ACKNOWLEDGMENTS

We are grateful to Steve Allen, Gary Porter, Max Fenstermacher, Ilon Joseph, Ron Waltz, Jim Callen, Tom Rognlien, Xueqiao Xu, and the DIII-D Collaboration for helpful discussions and support in this work. The simulations made use of resources at the National Energy Research Supercomputer Center under Department of Energy Contract No. DE-AC03-76SF00098. This work was performed under the auspices of the U. S.

Department of Energy under Contract No. DE-AC52-07NA27344 at the Lawrence Livermore National Laboratory, Grant DE-FG02-07ER54917 at University of California San Diego, Grant DE-FG02-08ER54999 at the University of Wisconsin-Madison, and Grant DE-FC02-04ER54698 at General Atomics

Figure Captions

Figure 1. Root-mean-square (RMS) with respect to *Z* dependence of the ion density, electron temperature, and electrostatic potential at the separatrix in the outer midplane vs. time for Cases 4 and 5 simulations of shot #119919. (color on-line)

Figure 2. Shot #119919 (a) RMS ion density fluctuation vs. R and Z at saturation for Case 4 simulation of #119919; (b) RMS ion density fluctuations vs. R in the midplane for Cases 4 and 5; and (c) ratio of the RMS ion density fluctuation to the background ion density vs. R in the midplane for Cases 4 and 5. (color on-line)

Figure 3. Shot #119919 (a) RMS electron temperature fluctuation vs. R and Z at saturation for Case 4 simulation; (b) RMS electron temperature fluctuation vs. R in the midplane for Cases 4 and 5; and (c) ratio of the RMS electron temperature fluctuation to the background electron temperature vs. R in the midplane for Cases 4 and 5. (color on-line)

Figure 4. Shot #119919 (a) RMS particle flux vs. R and Z at saturation for Case 4 simulation; (b) RMS particle flux vs. R in the midplane for Cases 4 and 5; (c) RMS particle diffusion coefficient vs. R and Z for Cases 4 and 5; and (d) RMS particle diffusion coefficient vs. R in the midplane for Cases 4 and 5. (color on-line)

Figure 5. Shot #119919 (a) RMS electron conductive thermal flux vs. R in the midplane at saturation for Cases 4 and 5 simulation; (b) RMS electron conductive diffusion coefficient vs. R and Z for Cases 4; and (c) electron conductive thermal diffusion coefficient vs. R in the midplane for Cases 4 and 5. (color on-line)

Figure 6. Comparison to probe data (green) to Case 5 simulation (red) of shot #119919 for (a) electron density and (b) electron temperature fluctuations, (c) radial particle flux, and (d) total electron radial heat flux vs. probe radius position near midplane. (color on-line)

Figure 7. Shot #119919/119921. Comparison of BES data (green) to synthetic diagnostics for Case 5 simulation (red) for (a) relative electron density vs. radius near midplane, (b0 density correlation function vs. ΔZ separation, and (c) density fluctuation power spectrum vs. frequency. (color on-line)

Figure 8. Shot #119919/119921. Model fit of radial electric field E_r vs. radius in midplane to (a) probe and (b) CER data, and (c) the shearing rate dV_{ExB}/dr vs. radius implied by the fitted E_r. (color on-line)

Figure 9. Shot #119919. (a) Case 1 with/without E_r simulation histories for RMS ion density and electric potential fluctuations at the separatrix and in the midplane vs. time. (b) Case 4, 5, and 6 simulation histories for the RMS ion density, electric potential, and electron temperature fluctuations at the separatrix and in the miplane vs time. (color on-line)

Figure 10. Shot #119919. (a) Case 5 (E_r=0) simulation RMS ion density, radial particle flux, and electron temperature fluctuations vs. radius in the midplane compared to probe data (diamonds). (b) Case 6 (with E_r) simulation RMS ion density, radial particle flux, and electron temperature fluctuations vs. radius in midplane compared to probe data (diamonds). (color on-line)

Figure 11. (a) Ion density and (b) electron temperature radial profiles in midplane for shots #119919, 119930, and 119934. (color on-line)

Figure 12. Comparison of probe data for (a) electron density and (b) electron temperature fluctuations, (c) radial particle flux, and (d) total electron radial heat flux vs. probe position near midplane data for shots #119919 (red), 119930 (green), and 119934 (blue). (color on-line)

Figure 13. Histories of the RMS ion density, electric potential, and electron temperature fluctuations at the separatrix and in the midplane in Case 4 simulations of shots #119919 (solid line) and colder, lower density plasma 119934 (dashed line). (color on-line)

Figure 14. Comparison of probe data (dark green) and Case 5 (red) and Case 6 (green) simulation data for (a) electron density and (b) electron temperature fluctuations, (c) radial particle flux, and (d) total electron radial heat flux vs. probe position near midplane data for shot #119934. (color on-line)

Figure 15. RMS radial particle flux, conductive and convective radial thermal fluxes vs. radius in the midplane compared to probe data (diamonds) for Case 5 (E_r=0) simulations of shots (a) #119919 and (b) colder, lower density plasma #119934. (color on-line)

Figure 16. Model fit of radial electric field E_r vs. radius in midplane to probe and CER data for shot #119934. (color on-line)

Figure 17. Cases 5 (E_r=0) and 6 (with E_r) simulation data for histories of the RMS (a) ion density, (b) electron temperature, and (c) electric potential fluctuations at the separatrix in the midplane for shot #119934. (color on-line)

Table I. Comparison of BOUT simulations with probe data for DIII-D shot #119919

(peak values)

BOUT simulation Case No.	$<\delta N_i>_{rms}$ [$10^{18}m^{-3}$]	$<\delta T_e>_{rms}$ [eV]	Radial Particle Flux [$10^{20}/m^2s$]	D_r [m^2/s]	Radial Conductive Heat Flux [$10^{20}/m^2s$]	χ_e [m^2/s] Cond.	Radial Total Heat Flux [$10^3 J/m^2s$]	χ_e [m^2/s] Total
#1: $\delta T_e=0$ w/E_r**	0.95 0.37	N/A N/A	1.8 0.07	0.4 0.02	N/A N/A	N/A N/A	-- --	-- --
#2: $\delta T_e\neq0$ $\kappa^e_{\parallel}=0$	1.0	43	4.3	0.77	54	7.2	-- --	-- --
#3: $\delta T_e\neq0$ $\kappa^e_{\parallel}\neq0$	0.58	5.8	1.0	0.17	0.72	0.2	-- --	-- --
#4: $\delta T_e\neq0$ $\kappa^e_{\parallel}\neq0$ & $\tilde{\mathbf{b}}\cdot\nabla$	1.3	4.0	3.3	1.7	3.3	2.7	-- --	-- --
#5:$\delta T_{e,i}\neq0$	2.0	7.5	9.5	2.0	10	2.2	22	4
#6:$\delta T_{e,i}\neq0$ w/E_r w/5E_r	0.7 0.3	5.5 3.5	0.8 0.18	0.27 0.035	2.5 0.75	0.32 0.036	4.6	0.39
DIII-D #119919 probe data	2.0	10	11	0.2-1 ‡	1.2	~1-2 ‡	12	1-3 ‡

**Cases #1 w/E_r has not saturated at end of simulation (1.8 ms)
‡Typical, flux-surface-averaged values for shot #119919 inferred from UEDGE reconstruction

Table II. Comparison of BOUT simulations with BES data for DIII-D shot #119919

BOUT simulation Case No.	$<\delta N_i/N_i>_{rms}$ peak vs. R raw/filtered	$\Delta R_{half\text{-}max}$ [cm] of $<\delta N_i/N_i>_{rms}$ raw/filtered	$\Delta Z_{corr,half\text{-}max}$ [cm] of density raw/filtered	Peak freq [10^5 rad/s] in density fluct'n spect raw/filtered	$\Delta\omega_{half\text{-}max}$ [10^5 rad/s] in density fluct'n spect, raw/filtered
#1: $\delta T_e=0$ w/E_r **	0.13 / 0.07 0.065/0.045	1.2 / 1.5 0.7 / 0.8	0.6 / 0.9 2.0 / 2.3	3 / 0.5 0 / 0	4 / 2 1/ 0.7
#2: $\delta T_e\neq 0$ $\kappa^e_{\parallel}=0$	0.25 / 0.12	1.1 / 1.2	0.5 / 1.2	0 / 0	1.5 / 1
#3: $\delta T_e\neq 0$ $\kappa^e_{\parallel}\neq 0$	0.17 / 0.08	1.7 / 1.9	0.4 / 1.4	0 / 0	1.5 / 1
#4: $\delta T_e\neq 0$ $\kappa^e_{\parallel}\neq 0$ & $\tilde{\mathbf{b}}\cdot\nabla$	0.20 / 0.12	1.4 / 1.2	0.6 / 2	0 / 0	3.5 / 3
#5:$\delta T_{e,i}\neq 0$	0.21 / 0.12	1.7 / 2	0.4 / 0.7	3.0 / 1.5	2 / 1.2
#6:$\delta T_{e,i}\neq 0$ w/E_r w/5E_r	0.07 / 0.05 0.011/0.006	1.5 / 1.7 0.5 / 0.6	0.8 / 0.9 3 / 3	0.5 / 0.5 3.8 / 3.8	0.5 / 0.5 0.25 / 0.25
DIII-D #119919 probe data	0.09±0.2	2±0.2	2±0.2	3.8	1.32±0.2

**Cases #1 w/E_r has not saturated at end of simulation (1.8 ms)

Figure 1

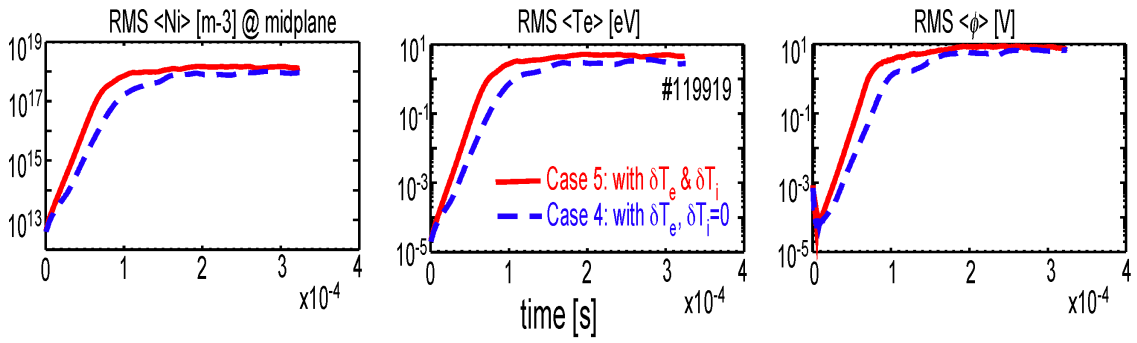
RMS <Ni> [m-3] @ midplane
RMS <Te> [eV]
RMS <ϕ> [V]
#119919
Case 5: with δTe & δTi
Case 4: with δTe, δTi=0
time [s]
x10-4

Figure 2

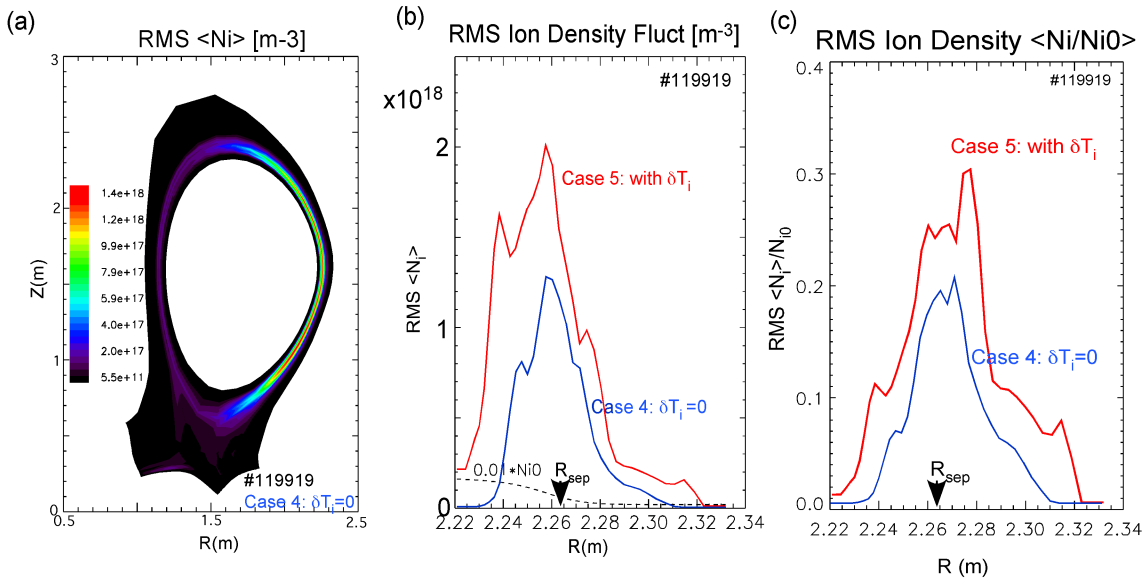
(a)
RMS <Ni> [m-3]
1.4e+18
1.2e+18
9.9e+17
7.9e+17
5.9e+17
4.0e+17
2.0e+17
5.5e+11
Z(m)
R(m)
#119919
Case 4: δTi=0
(b)
RMS Ion Density Fluct [m-3]
x10^18
#119919
Case 5: with δTi
Case 4: δTi=0
0.01*Ni0
Rsep
RMS <Ni>
R(m)
(c)
RMS Ion Density <Ni/Ni0>
#119919
Case 5: with δTi
Case 4: δTi=0
Rsep
RMS <Ni>/Ni0
R (m)

Figure 3

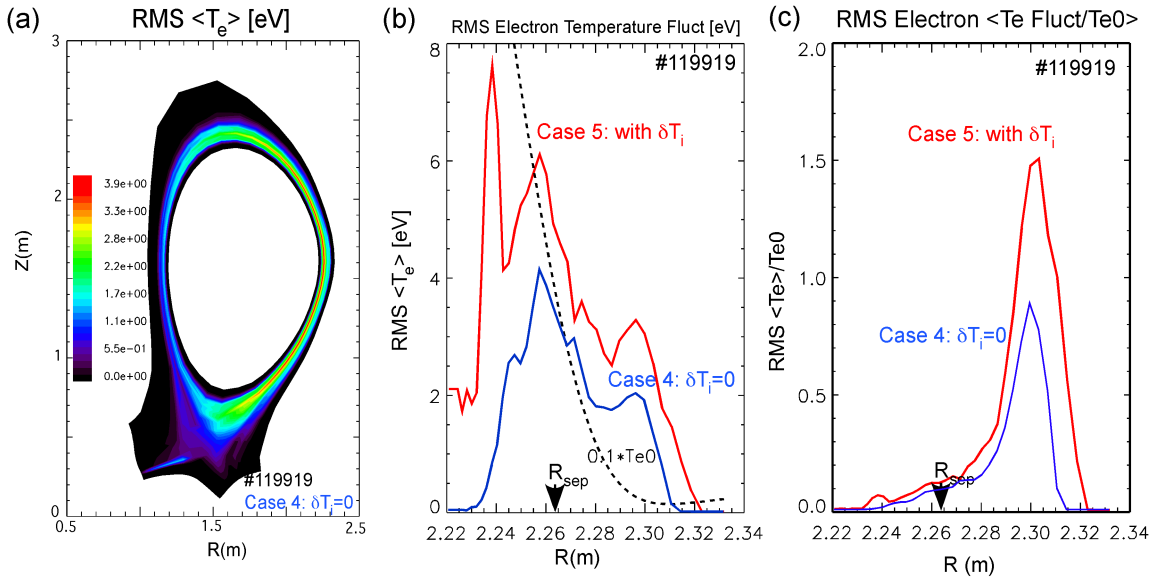
(a)
RMS <Te> [eV]
3.9e+00
3.3e+00
2.8e+00
2.2e+00
1.7e+00
1.1e+00
5.5e-01
0.0e+00
#119919
Case 4: δTi=0
Z(m)
R(m)
(b)
RMS Electron Temperature Fluct [eV]
#119919
Case 5: with δTi
Case 4: δTi=0
0.1*Te0
Rsep
RMS <Te> [eV]
R(m)
(c)
RMS Electron <Te Fluct/Te0>
#119919
Case 5: with δTi
Case 4: δTi=0
Rsep
RMS <Te>/Te0
R (m)

Figure 4

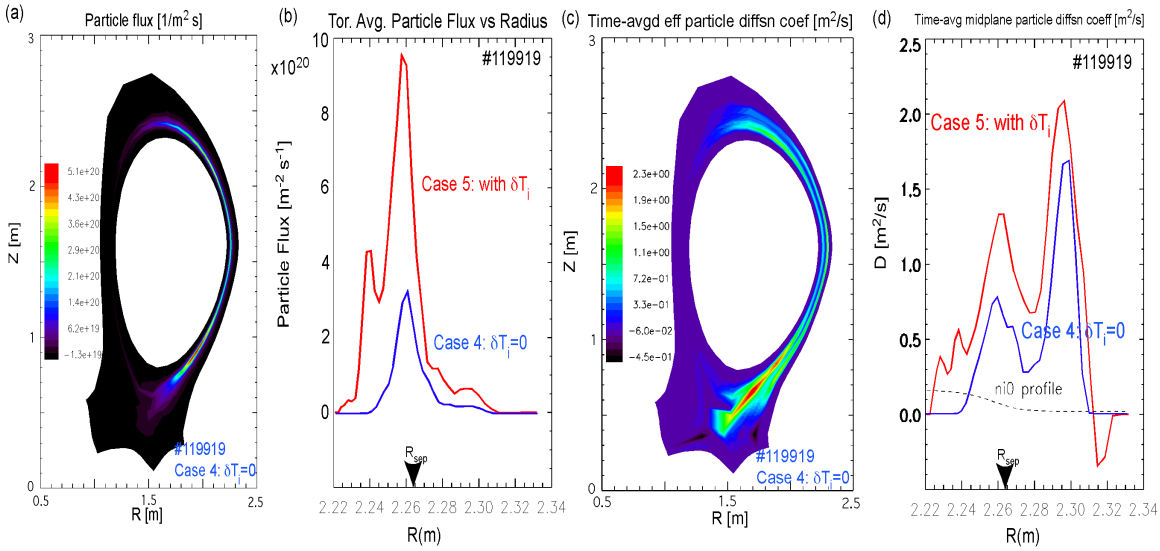
(a)
Particle flux [1/m² s]
Z [m]
R [m]
#119919
Case 4: δTi=0
(b)
Tor. Avg. Particle Flux vs Radius
x10²⁰
Particle Flux [m⁻² s⁻¹]
#119919
Case 5: with δTi
Case 4: δTi=0
Rsep
R(m)
(c)
Time-avgd eff particle diffsn coef [m²/s]
Z [m]
R [m]
#119919
Case 4: δTi=0
(d)
Time-avg midplane particle diffsn coeff [m²/s]
D [m²/s]
#119919
Case 5: with δTi
Case 4: δTi=0
ni0 profile
Rsep
R(m)

Figure 5

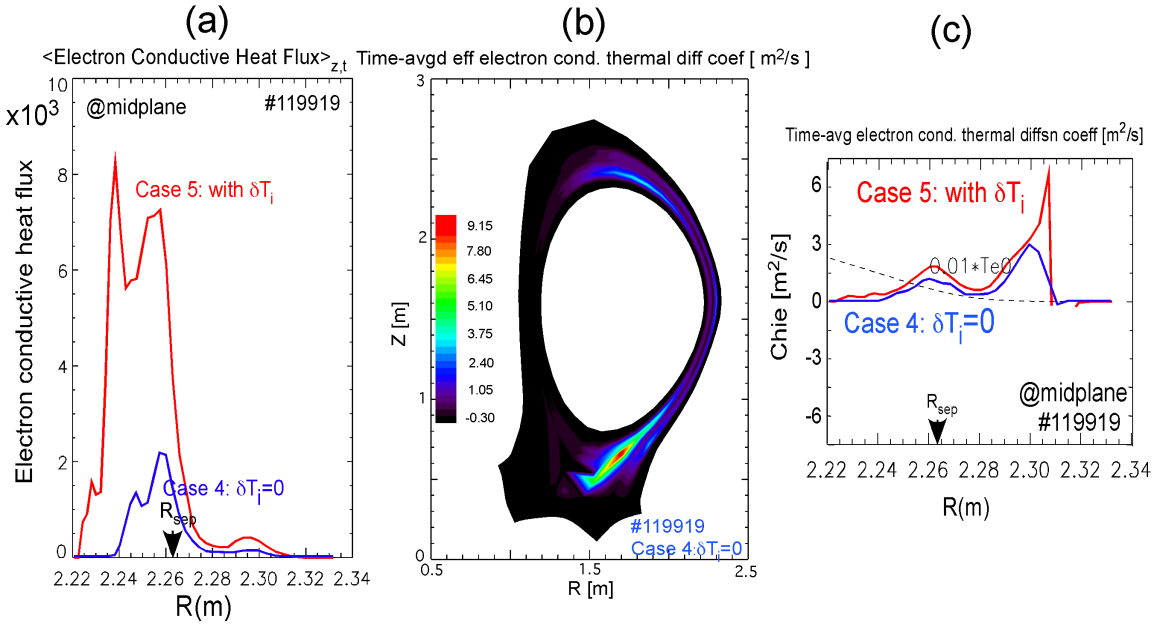
(a)
<Electron Conductive Heat Flux>z,t
x10^3
@midplane
#119919
Case 5: with δTi
Case 4: δTi=0
Rsep
Electron conductive heat flux
R(m)
(b)
Time-avgd eff electron cond. thermal diff coef [m2/s]
9.15
7.80
6.45
5.10
3.75
2.40
1.05
-0.30
Z [m]
R [m]
#119919
Case 4:δTi=0
(c)
Time-avg electron cond. thermal diffsn coeff [m2/s]
Case 5: with δTi
0.01*Te0
Case 4: δTi=0
Rsep
@midplane
#119919
Chie [m2/s]
R(m)

Figure 6

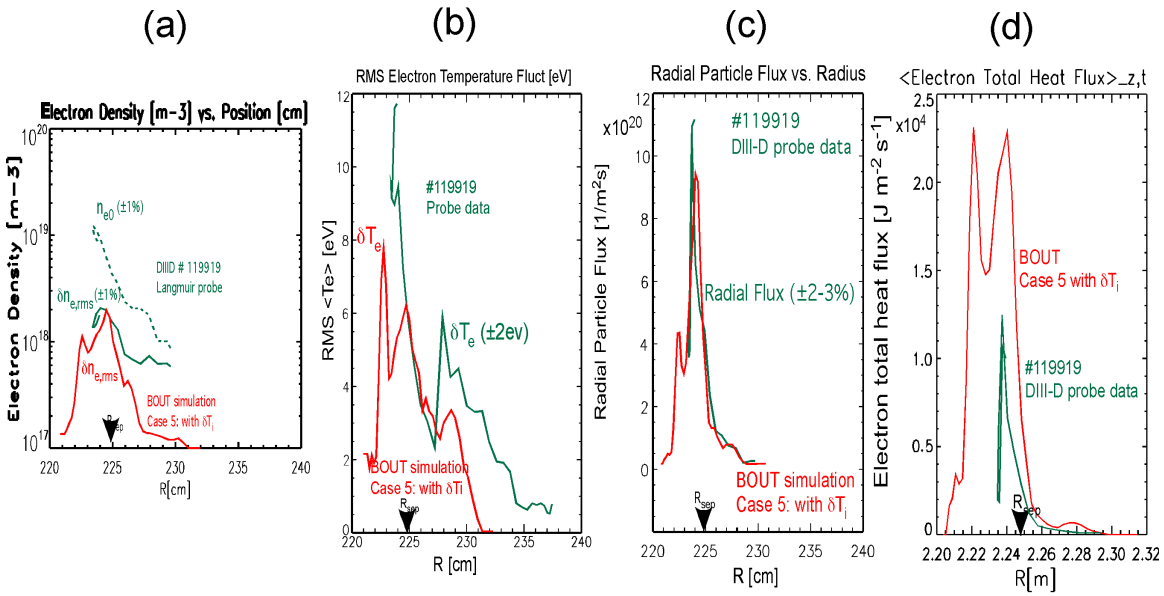
(a)
(b)
(c)
(d)
Electron Density [m-3] vs. Position [cm]
Electron Density [m-3]
R[cm]
DIIID # 119919
Langmuir probe
BOUT simulation
Case 5: with δT_i
RMS Electron Temperature Fluct [eV]
RMS <Te> [eV]
R [cm]
#119919
Probe data
δT_e (±2ev)
BOUT simulation
Case 5: with δTi
Radial Particle Flux vs. Radius
Radial Particle Flux [1/m²s]
#119919
DIII-D probe data
Radial Flux (±2-3%)
BOUT simulation
Case 5: with δT_i
R [cm]
<Electron Total Heat Flux>_z,t
Electron total heat flux [J m⁻² s⁻¹]
BOUT
Case 5 with δT_i
#119919
DIII-D probe data
R[m]

Figure 7

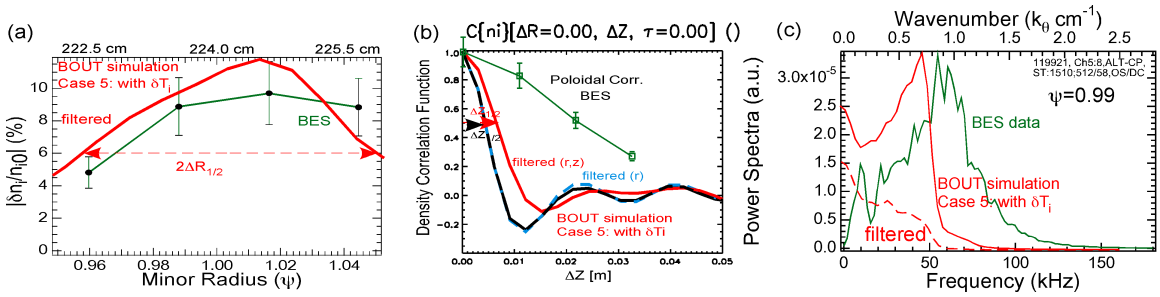
(a)
222.5 cm
224.0 cm
225.5 cm
BOUT simulation
Case 5: with δT_i
filtered
BES
2ΔR_1/2
|δn_i/n_0| (%)
Minor Radius (ψ)
(b)
C[ni][ΔR=0.00, ΔZ, τ=0.00] ()
Poloidal Corr.
BES
filtered (r,z)
filtered (r)
BOUT simulation
Case 5: with δTi
Density Correlation Function
ΔZ [m]
(c)
Wavenumber (k_θ cm^-1)
119921, Ch5:6,ALT-CP,
ST:1510;512/58,OS/DC
ψ=0.99
BES data
BOUT simulation
Case 5: with δT_i
filtered
Power Spectra (a.u.)
Frequency (kHz)

Figure 8

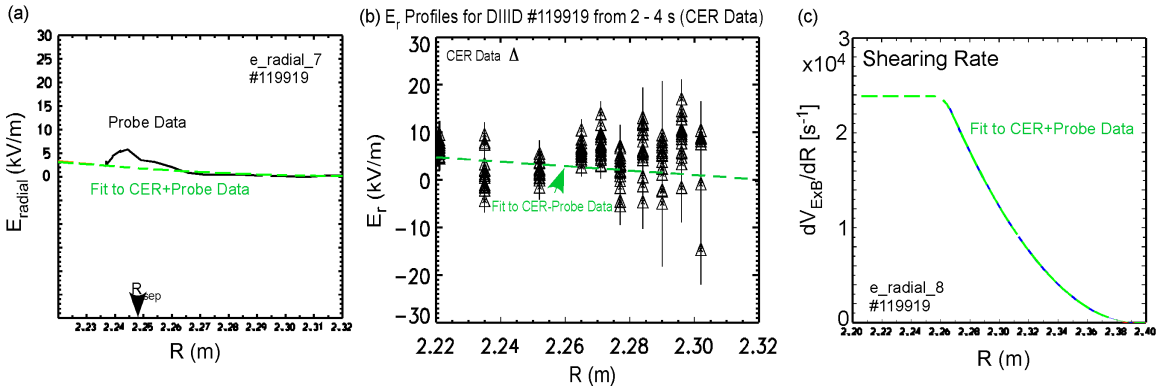
(a)
e_radial_7
#119919
Probe Data
Fit to CER+Probe Data
R_{sep}
E_{radial} (kV/m)
R (m)
(b) E_r Profiles for DIIID #119919 from 2 - 4 s (CER Data)
CER Data Δ
Fit to CER-Probe Data
E_r (kV/m)
R (m)
(c)
Shearing Rate
x10^4
Fit to CER+Probe Data
e_radial_8
#119919
dV_{ExB}/dR [s^{-1}]
R (m)

Figure 9

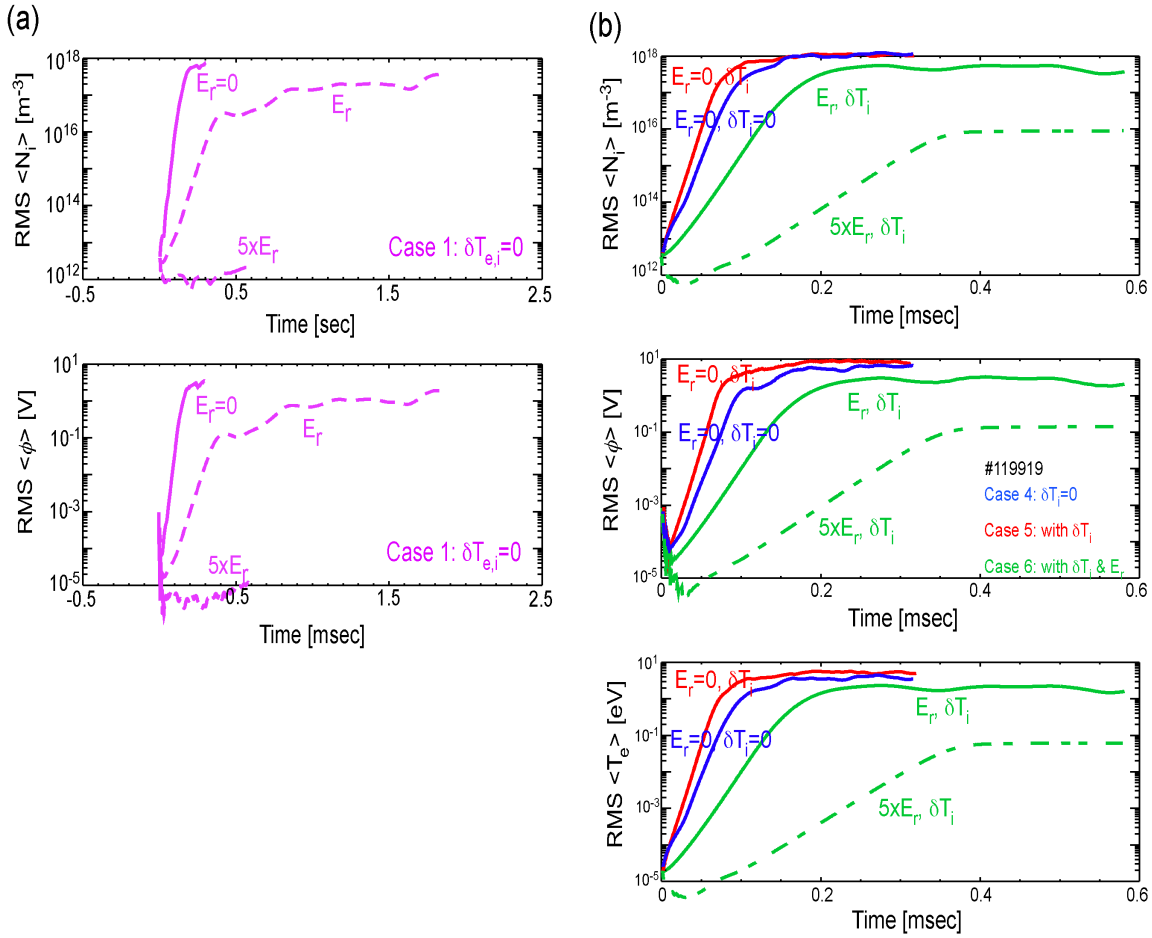
(a)
RMS <N_i> [m^-3]
E_r=0
E_r
5xE_r
Case 1: δT_e,i=0
Time [sec]
RMS <φ> [V]
E_r=0
E_r
5xE_r
Case 1: δT_e,i=0
Time [msec]
(b)
RMS <N_i> [m^-3]
E_r=0, δT_i
E_r=0, δT_i=0
E_r, δT_i
5xE_r, δT_i
Time [msec]
RMS <φ> [V]
E_r=0, δT_i
E_r=0, δT_i=0
E_r, δT_i
5xE_r, δT_i
#119919
Case 4: δT_i=0
Case 5: with δT_i
Case 6: with δT_i & E_r
Time [msec]
RMS <T_e> [eV]
E_r=0, δT_i
E_r=0, δT_i=0
E_r, δT_i
5xE_r, δT_i
Time [msec]

Figure 10

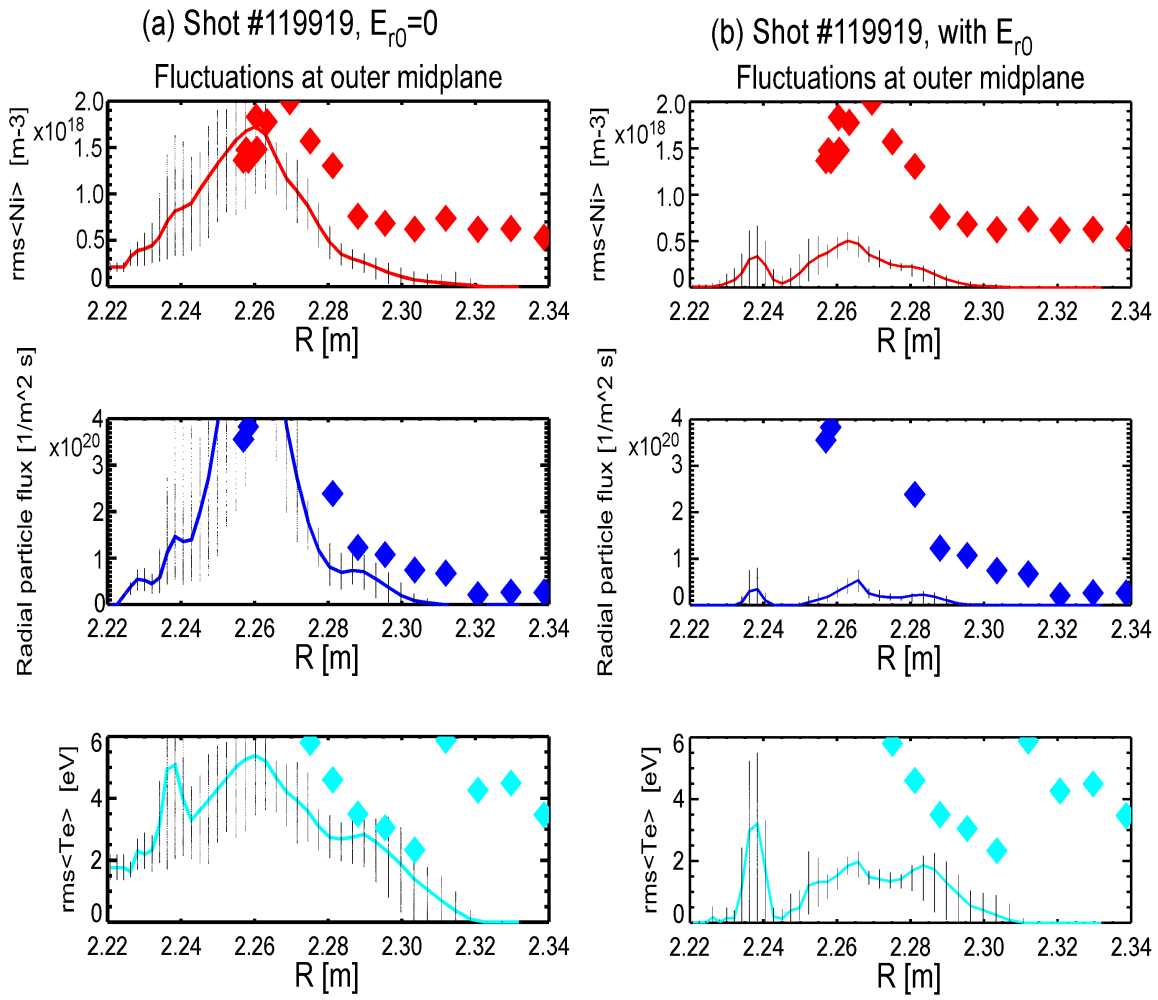
(a) Shot #119919, E_{r0}=0
Fluctuations at outer midplane
(b) Shot #119919, with E_{r0}
Fluctuations at outer midplane
rms<Ni> [m-3]
x10^18
Radial particle flux [1/m^2 s]
x10^20
rms<Te> [eV]
R [m]

Figure 11

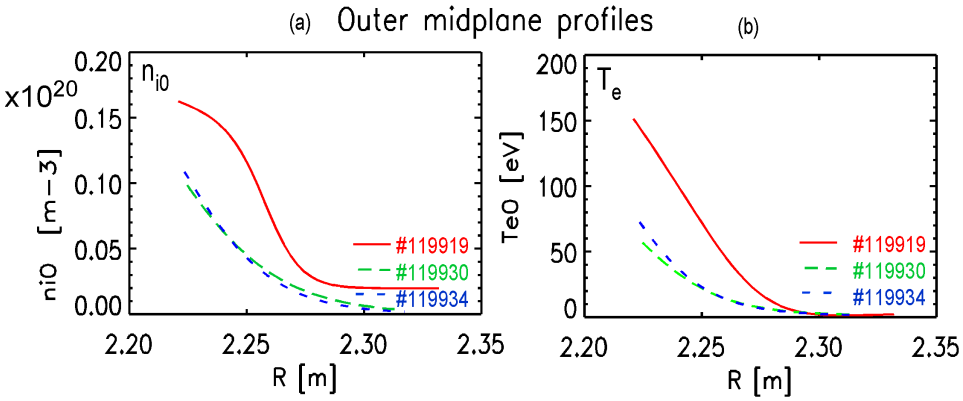
(a) Outer midplane profiles
(b)
n_{i0}
x10^20
niO [m-3]
0.20
0.15
0.10
0.05
0.00
2.20
2.25
2.30
2.35
R [m]
#119919
#119930
#119934
T_e
TeO [eV]
200
150
100
50
0
2.20
2.25
2.30
2.35
R [m]
#119919
#119930
#119934

Figure 12

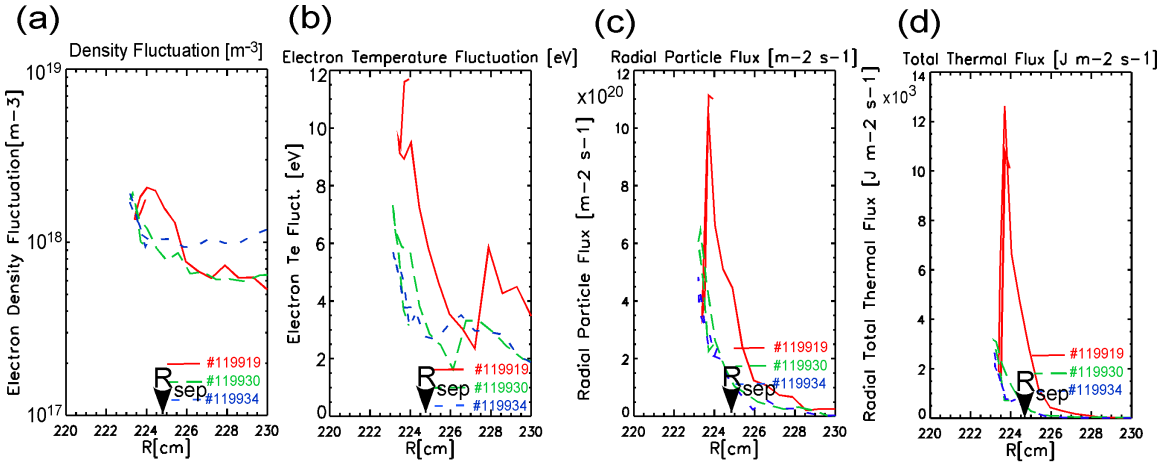
(a)
Density Fluctuation [m-3]
Electron Density Fluctuation[m-3]
R[cm]
#119919
#119930
#119934
Rsep
(b)
Electron Temperature Fluctuation [eV]
Electron Te Fluct. [eV]
R[cm]
(c)
Radial Particle Flux [m-2 s-1]
x10^20
Radial Particle Flux [m-2 s-1]
R[cm]
(d)
Total Thermal Flux [J m-2 s-1]
x10^3
Radial Total Thermal Flux [J m-2 s-1]
R[cm]

Figure 13

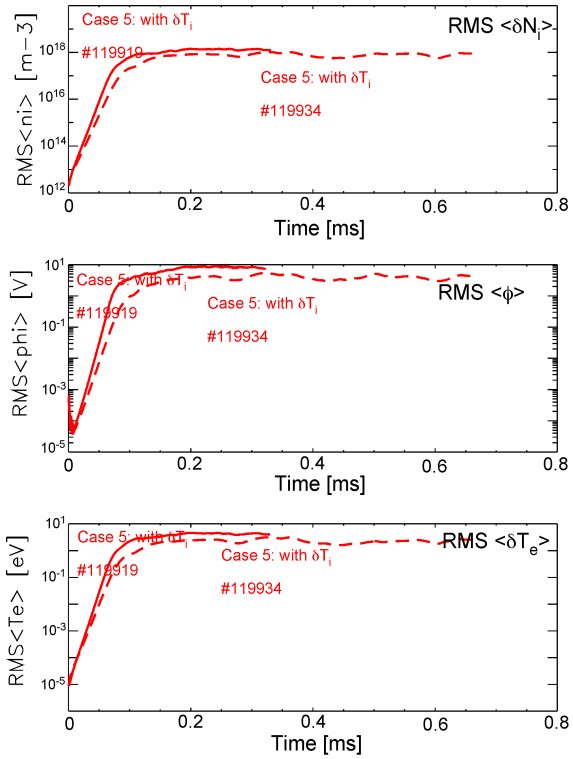
Case 5: with δT_i
#119919
Case 5: with δT_i
#119934
RMS <δN_i>
RMS<ni> [m−3]
Time [ms]
Case 5: with δT_i
#119919
Case 5: with δT_i
#119934
RMS <ϕ>
RMS<phi> [V]
Time [ms]
Case 5: with δT_i
#119919
Case 5: with δT_i
#119934
RMS <δT_e>
RMS<Te> [eV]
Time [ms]

Figure 14

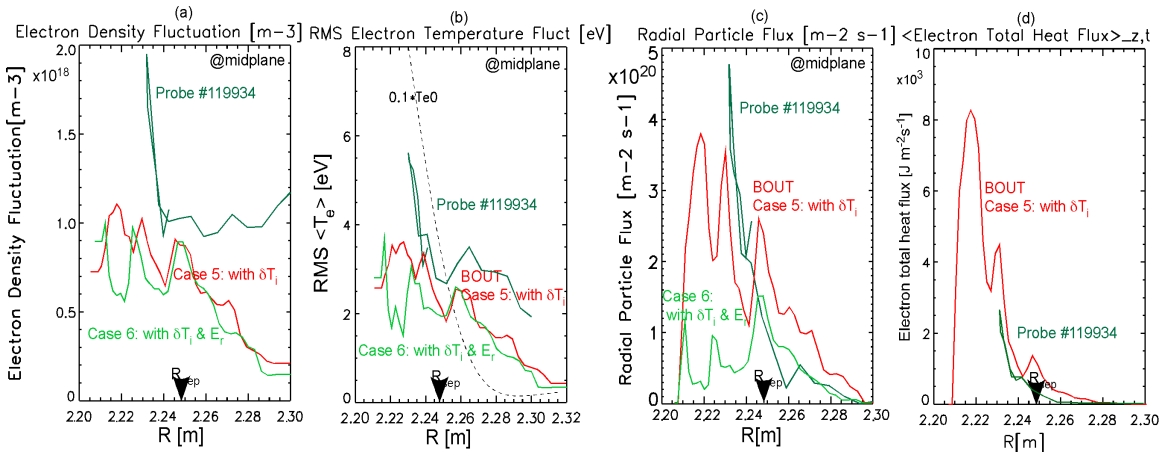
(a)
Electron Density Fluctuation [m−3]
@midplane
Probe #119934
Case 5: with δT_i
Case 6: with δT_i & E_r
R_sep
Electron Density Fluctuation[m−3]
x10^18
R [m]
(b)
RMS Electron Temperature Fluct [eV]
@midplane
0.1*Te0
Probe #119934
BOUT
Case 5: with δT_i
Case 6: with δT_i & E_r
RMS <T_e> [eV]
R [m]
(c)
Radial Particle Flux [m−2 s−1]
@midplane
Probe #119934
BOUT
Case 5: with δT_i
Case 6:
with δT_i & E_r
Radial Particle Flux [m−2 s−1]
x10^20
R[m]
(d)
<Electron Total Heat Flux>_z,t
BOUT
Case 5: with δT_i
Probe #119934
Electron total heat flux [J m^−2s^−1]
x10^3
R[m]

Figure 15

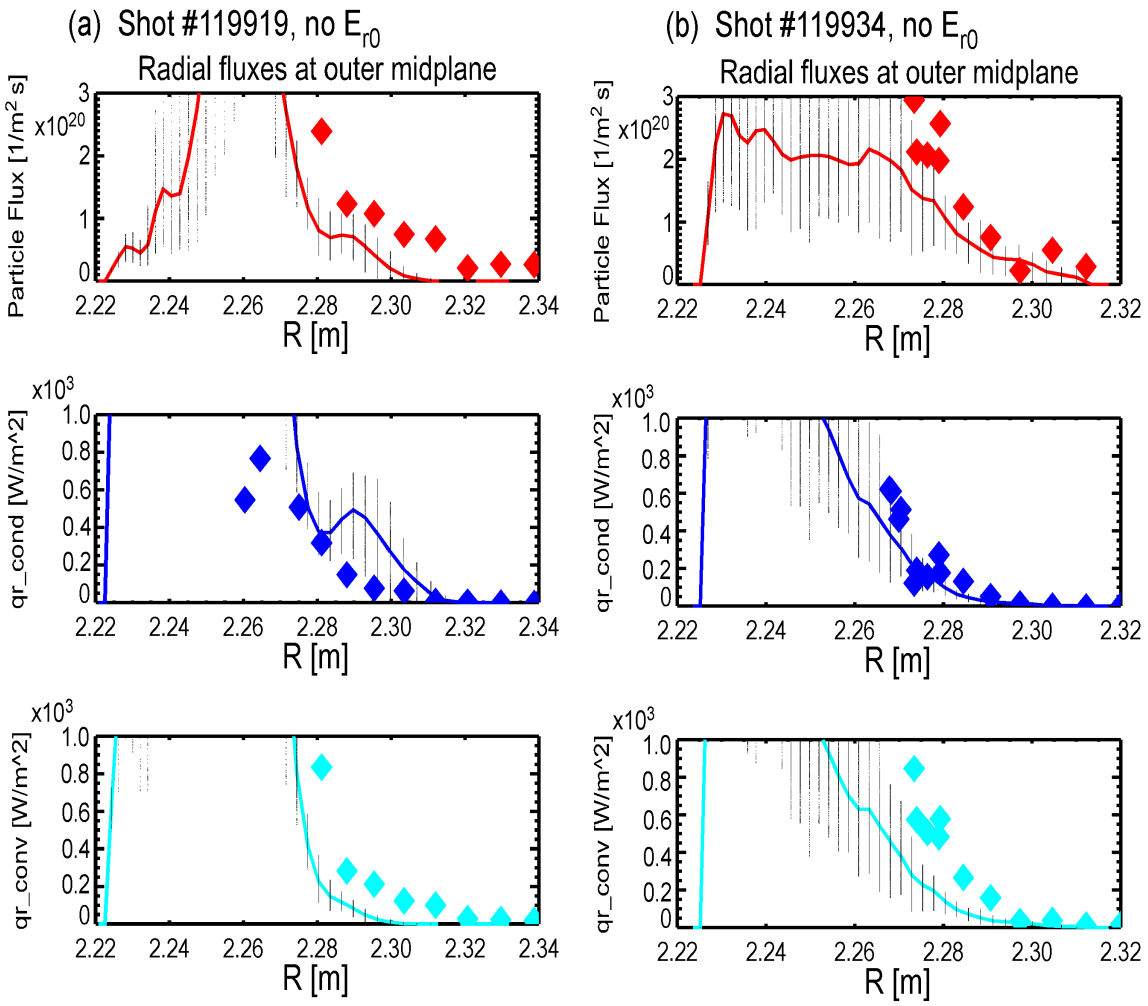
(a) Shot #119919, no E_{r0}
Radial fluxes at outer midplane
Particle Flux [1/m^2 s]
x10^{20}
R [m]
qr_cond [W/m^2]
x10^3
qr_conv [W/m^2]
(b) Shot #119934, no E_{r0}
Radial fluxes at outer midplane

Figure 16

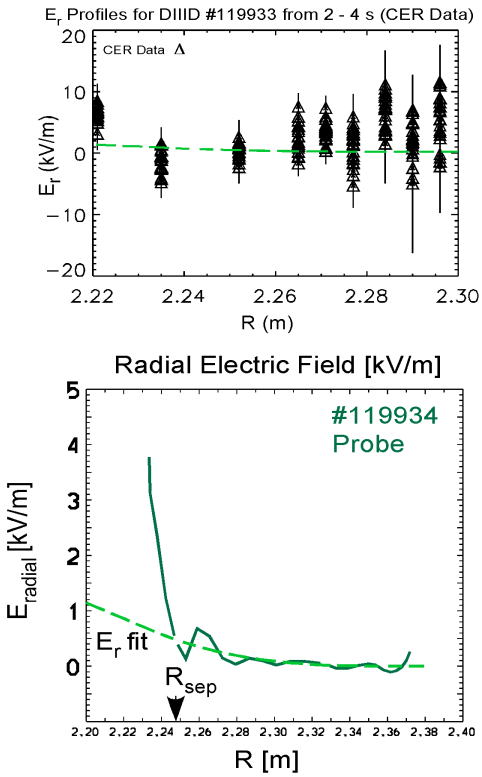
E_r Profiles for DIIID #119933 from 2 - 4 s (CER Data)
CER Data
E_r (kV/m)
R (m)
Radial Electric Field [kV/m]
#119934
Probe
E_r fit
R_sep
E_radial [kV/m]
R [m]

Figure 17

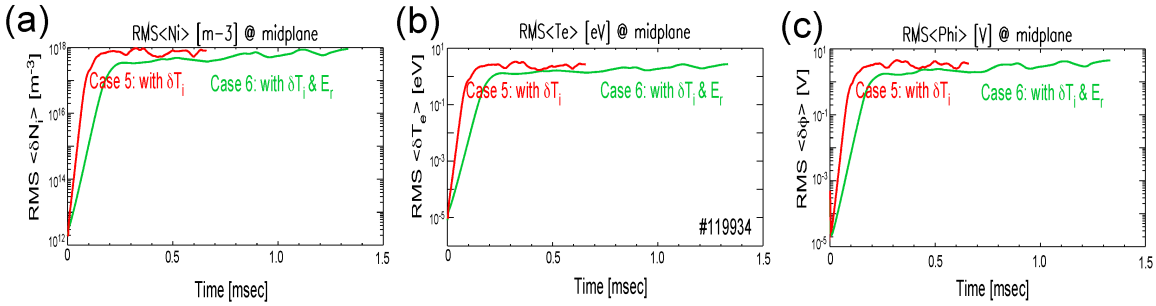
(a)
RMS<Ni> [m-3] @ midplane
RMS <δN_i> [m^-3]
Case 5: with δT_i
Case 6: with δT_i & E_r
Time [msec]
(b)
RMS<Te> [eV] @ midplane
RMS <δT_e> [eV]
Case 5: with δT_i
Case 6: with δT_i & E_r
#119934
Time [msec]
(c)
RMS<Phi> [V] @ midplane
RMS <δφ> [V]
Case 5: with δT_i
Case 6: with δT_i & E_r
Time [msec]

[1] J.E. Kinsey, G. Bateman, T. Onjun et al, Nucl. Fusion **43,** 1845 (2003).

[2] M. Kotschenreuther, P. M. Valanju, S. M. Mahajan, and J. C. Wiley, Phys. Plasmas **14**, 072502 (2007).

[3] J. L. Luxon, T. C. Simonen, R. D. Stambaugh, and DIII-D Team, Fusion Sci. Technol. **48**, 807 (2002).

[4]A. J. Wooton, B. A. Carreras, H. Matsumoto, K. McGuire, W. A. Peebles, Ch. P. Ritz, P. W. Terry, and S. J. Zweben, Phys. Fluids B **2**, 2879 (1990).

[5]B. A. Carreras, P. H. Diamond, M. Murakami, J. L. Dunlap, J. D. Bell, H. R. Hicks, J. A. Holmes, E. A. Lazarus, V. K. Pare, P. Similon, C. E. Thomas, R. M. Wieland, Phys. Rev. Lett. **50**, 503 (1983).

[6]B. A. Carreras, L. Garcia, and P. H. Diamond, Phys. Fluids **30**, 1388 (1987).

[7]P. N. Guzdar, J. F. Drake, D. McCarthy, A. B. Hassam, and C. S. Liu, Phys. Fluids B **5**, 3712 (1993).

[8]S. V. Novakovskii, P. N. Guzdar, J. F. Drake, and C. S. Liu, Phys. Plasmas 2, 3764 (1995).

[9]P. N. Guzdar and A. B. Hassam, Phys. Plasmas **3**, 3701 (1996).

[10]B. N. Rogers, J. F. Drake, and A. Zeiler, Phys. Rev. Lett. **81**, 4396 (1998).

[11]P. N. Guzdar, R. G. Kleva, R. J. Groebner, and P. Gohil, Phys. Plasmas **11**, 1109 (2004).

[12]H. P. Furth, J. Killeen, and M. N. Rosenbluth, Phys. Fluids **6**, 77 (1963).

[13]B. Coppi, Phys. Fluids **7**, 1501 (1964).

[14]X. Q. Xu, and R. H. Cohen, Contrib. Plasma Phys. 36 (1998) 158; X. Q. Xu, R. H. Cohen, T. D. Rognlien, and J. R. Myra, Phys. Plasmas 7, 1951 (2000).

[15]M.V. Umansky, X.Q. Xu, B. Dudson, L.L. LoDestro and J.R. Myra, Comp. Phys. Commun. **180**, 887 (2008).

[16]B. D. Dudson, M. V. Umansky, X. Q. Xu, P. B. Snyder, and H. R. Wilson, Comp. Phys. Commun. **180**, 1467 (2009).

[17]J. Boedo, D. Rudakov, R.A. Moyer, S. Krasheninnikov, D.G. Whyte, G.R. Mckee, G. Tynan, M. Schaffer, P.G. Stangeby, and P. West, Phys. Plasmas 8, 4826 (2001); J. Boedo, N. Crocker, L. Chousal, R. Hernandez, J. Chalfant, H.W. Kugel, P. Roney, J. Wertenbaker, and Nstx Team, Rev. Sci. Instrum. 80, 123506 (2009).

[18]D. Gupta, R. Fonck, G. McKee, D. Schlossberg, and M. Shafer, Rev. Sci. Instrum. **75**, 3493 (2004); G. R. McKee, R. J. Fonck, M. W. Shafer, I. U. Uzun-Kaymak IU, Z. Yan, Rev Sci Instrum. **81**, 10D741 (2010); G.R. McKee1, P. Gohil, D. J. Schlossberg, J. A. Boedo, K. H. Burrell, J.S. deGrassie, R. J. Groebner, R.A. Moyer, C.C. Petty, T.L. Rhodes, L. Schmitz, M.W. Shafer, W.M. Solomon, M. Umansky, G. Wang, A.E. White, and X. Xu, Nucl. Fusion **49,** 115016 (2009).

[19]S. Braginskii, "Transport Processes in a Plasma," in Reviews of Plasma Physics, Vol. 1, ed. M. A. Leontovich (Consultants Bureau, New York, 1965), p. 205.

[20]B. D. Scott, Plasma Phys. Control. Fusion 49, S25 (2007).

[21]T. Rafiq, C. C. Hegna, J. D. Callen, and A. H. Kritz, Phys. Plasmas **16**, 102505 (2009).

[22]X. Q. Xu, M. V. Umansky, B. Dudson, and P. B. Snyder, Comm. Comp. Phys. 4, 949 (2008)

[23]T.D. Rognlien, J L. Milovich, M. E. Rensink, and G.D. Porter," J. Nucl. Mater. 196-198, 347 (1992).

[24]D. A. Baver, J. R. Myra and M.V. Umansky, Comp. Phys. Comm. **182**, 1610 (2011).

[25]P. H. Diamond, S.-I. Itoh, and K. Itoh, Modern Plasma Physics, (Cambridge University Press, Cambridge, U.K., 2010).

[26]J. L. Terry, S. J. Zweben, K. Hallatschek, B. LaBombard, R. J. Maqueda, B. Bai, C. J. Boswell, M. Greenwald, D. Kopon, W. M. Nevins, C. S. Pitcher, B. N. Rogers, D. P. Stotler, and X. Q. Xu, Phys. Plasmas 10, 1739 (2003)

[27]W.M. Nevins, "GKV User's Manual", UCRL-TR-206016 (Aug. 2004); W.M. Nevins et al., Phys. Plasmas 13, 122306 (2006).

[28]M. Groth, G. D. Porter, T. D. Rognlien, S. Wiesen, M. Wischmeier, M. N. A. Beurskens, X. Bonnin, B. D. Bray, S. Brezinsek, N. H. Brooks, D. P. Coster, T. Eich, M. E. Fenstermacher, C. Fuchs, R. A. Groebner, D. Harting, A. Huber, S. Jachmich, A. Kallenbach, C. J. Lasnier, A. W. Leonard, A. Meigs, H. W. Muller, M. E. Rensink, D. L. Rudakov, J. G. Watkins, E. Wolfrum, the DIII-D and ASDEX Upgrade Teams, and JET EFDA Contributors, Plasma Phys. Control. Fusion **53,** 124017 (2011); M. Groth, S. L. Allen, J. A. Boedo, N. H. Brooks, J. D. Elder, M. E. Fenstermacher, R. J. Groebner, C. J. Lasnier, A. G. McLean, A. W. Leonard, S. Lisgo, G. D. Porter, M. E. Rensink, T. D. Rognlien, D. L. Rudakov, P. C. Stangeby, W. R. Wampler, J. G. Watkins, W. P. West, and D. G. Whyte, Phys. Plasmas 14, 056120 (2007); G. D. Porter, private communication.

[29]P. Gohil, K. H. Burrell, R. J. Groebner, J. Kim, W. C. Martin, E. L. McKee, R. P. Seraydarian, "The charge exchange recombination diagnostic system on the DIII-D

tokamak", Proceedings of the 14th IEEE/NPSS Symposium on Fusion Engineering, 1991, vol. 2, p. 1199-1204 (30 Sep – 3 Oct 1991); P. Gohil, K. H. Burrell, T. N. Carlstrom, Nucl. Fusion 38, 1998, 93.

[30]T. S. Hahm and K. H. Burrell, Phys. Plasmas **2**, 1648 (1995)

[31]R. E. Waltz, J. M. Candy, and M. N. Rosenbluth, Phys. Plasmas 9, 1938 (2002); R. E. Waltz, J. Candy, F. L. Hinton, C. Estrada-Mila and J. E. Kinsey, Nucl. Fusion 45, 741 (2005).